



# Collective transport and reconfigurable assembly of nematic colloids by light-driven cooperative molecular reorientations

Jinghua Jiang<sup>a,1</sup>, Xinyu Wang<sup>b,1</sup>, Oluwafemi Isaac Akomolafe<sup>c,1</sup>, Wentao Tang<sup>b</sup>, Zhawure Asilehan<sup>a</sup>, Kamal Ranabhat<sup>c</sup> , Rui Zhang<sup>b,2</sup> , and Chenhui Peng<sup>a,2</sup>

Edited by Noel Clark, University of Colorado Boulder, Boulder, CO; received December 22, 2022; accepted March 9, 2023

Nanomotors in nature have inspired scientists to design synthetic molecular motors to drive the motion of microscale objects by cooperative action. Light-driven molecular motors have been synthesized, but using their cooperative reorganization to control the collective transport of colloids and to realize the reconfiguration of colloidal assembly remains a challenge. In this work, topological vortices are imprinted in the monolayers of azobenzene molecules which further interface with nematic liquid crystals (LCs). The light-driven cooperative reorientations of the azobenzene molecules induce the collective motion of LC molecules and thus the spatiotemporal evolutions of the nematic disclination networks which are defined by the controlled patterns of vortices. Continuum simulations provide physical insight into the morphology change of the disclination networks. When microcolloids are dispersed in the LC medium, the colloidal assembly is not only transported and reconfigured by the collective change of the disclination lines but also controlled by the elastic energy landscape defined by the predesigned orientational patterns. The collective transport and reconfiguration of colloidal assemblies can also be programmed by manipulating the irradiated polarization. This work opens opportunities to design programmable colloidal machines and smart composite materials.

liquid crystal | colloids | nanomotors

Nanoscale molecular motors are ubiquitous in biological systems (1). Thousands of nanomotors consume energy and are orchestrated cooperatively to carry out mechanical work at much larger length scales (2). During these biological processes, biomolecular motors self-assemble into ordered organizations, and their cooperative actions promote certain reorganization, thus realizing essential biological functions, such as motility, division, and replication of biological entities (2). For instance, the collective reorganization of protein motors in bacterial flagella, driven by consuming nearby nutrients, induces the rotation of flagella and thus the swimming of bacteria (3, 4). Molecular motor proteins can also drive the division of actin-based tactoid droplets (5). If one can mimic such nanomotor-engaged motions in nature with a self-organized composite in purely synthetic systems, man-made nanomachines that can collectively induce controlled motion of much larger objects would be feasible (6–9). To this end, great efforts have been made to synthesize such self-assembled molecular machines that can be collectively driven by external stimuli to perform work (10–12). In recent decades, light-driven molecular motors have been synthesized to control the motion of nanocars (13) and the rotation of microscale objects (14). In addition, the rotation of birefringent particles was demonstrated by harnessing optical angular momentum in high-power laser traps (15). Despite these successes, using the cooperative reconfiguration of self-assembled molecular-scale motors to control the motion and self-assembly of microscale colloids remains a grand challenge in the fields ranging from materials science to nanotechnology.

Azobenzene molecules and their derivatives, which are photosensitive to polarized light, have been synthesized and used as artificial motors (16). Liquid crystals (LCs), anisotropic media exhibiting long-range orientational order (17), have been used to control the self-assembly of colloids (18–30). Combining cooperatively driven azobenzene molecular motors with an LC medium has shown great potential in manipulating the motion of microscale colloids (31). Large-area optoelastic manipulation of colloids in the LC medium was demonstrated by using a monolayer of azobenzene molecules (25). Azobenzene-containing moieties have also been coated on colloids in the shape of hexagonal prisms (32, 33) and rods (34) to realize optically driven translation and rotation in LC. Another important direction is to directly mix chiral azobenzene molecular switches with nematic LC to form the so-called cholesteric LC (35). Along the winding/unwinding processes under light stimulation, the collective change in the helicity of the nanomotors triggers the rotation, translation, and aggregation of the colloidal rods (14, 36) and spheres (37). However, a

## Significance

The 2016 Nobel Prize in Chemistry has been awarded to the work on the design and synthesis of tiny molecular machines. How to utilize the cooperative action of the molecular motors to drive the collective motion of microscale objects remains a grand challenge. This work combines the light-driven molecular motors with liquid crystal (LC) molecules in the nematic phase whose orientations are programmed with topological patterns and disclination networks. Through light irradiation, the cooperative reorganizations of nanomotors induce collective dynamics of the disclination networks. The morphology changes of the disclination lines are utilized to transport and reconfigure the colloidal assemblies in translational, rotational, and programmable fashions. This work opens the door for future applications in micromachines and smart materials.

Author contributions: C.P. conceived the research; J.J., O.I.A., K.R. and Z.A. performed the experiments; X.W., W.T. and R.Z. performed the numerical modelling; C.P. and R.Z. directed the research; J.J., and C.P. analysed the data; and J.J., and C.P. wrote the paper.

The authors declare no competing interest.

This article is a PNAS Direct Submission.

Copyright © 2023 the Author(s). Published by PNAS. This article is distributed under [Creative Commons Attribution-NonCommercial-NoDerivatives License 4.0 \(CC BY-NC-ND\)](#).

<sup>1</sup>J.J., X.W., and O.I.A. contributed equally to this work.

<sup>2</sup>To whom correspondence may be addressed. Email: ruzhang@ust.hk or cpeng2@ustc.edu.cn.

This article contains supporting information online at <https://www.pnas.org/lookup/suppl/doi:10.1073/pnas.2221718120/-DCSupplemental>.

Published April 11, 2023.

versatile method to control the collective transport of the colloidal assembly while realizing the reconfigurable self-assembly of the colloids by using the cooperative reorganization of the azobenzene molecules in LC remains elusive.

In this work, we propose to coat azobenzene molecules on two bounding surfaces for a slab of nematic LC. Each of them is photopatterned with different orientational patterns by using the maskless photopatterning method (38, 39). As such, disclination lines are formed in the LC due to the frustration from the different director fields on the bounding surfaces (40, 41). Specifically, a topological pattern is adopted and frozen by a liquid crystalline polymer on the bottom surface, and a uniform alignment is used on the top surface; as such, disclination lines are formed in the nematic bulk. Then, the top monolayer of azobenzene molecules is irradiated by linearly polarized light, and cooperative rotation of the molecular motors is induced, triggering the collective reorientation of the LC molecules; thus, the rotation and translation of the disclination lines depend on the topological patterns used on the bottom surface. Continuum simulations are conducted to reproduce these topological transformations and provide the three-dimensional (3D) director field of the system. The light-driven rotation–rotation and rotation–translation conversions can not only collectively transport the assembled

colloidal chains but also pick up individual colloids to form new colloidal assemblies. The reconfiguration of colloidal self-assembly on the disclination lines is then demonstrated by programming the morphology transformation of the disclination networks. The reconfigurable colloidal assemblies are controlled not only by the spatio-temporal evolutions of the disclination lines which can be realized through manipulating the irradiated polarization, but also by the elastic potential landscape defined by the designed director fields. The colloidal interactions during the self-assembly process on the disclination lines are also characterized. As such, the demonstrated effects in this work open the door for opto-mechanical devices and micromachines in the future.

## Results

**Rotation of Nematic Disclination Lines by Cooperative Rotation of Molecular Motors.** The azobenzene molecular motor used in this work is SD1, Fig. 1A, which is coated on cleaned glass substrates (*Methods*). As an example, the circular orientational pattern with +1 defect is imprinted on the substrates by a maskless photopatterning system (38, 40), Fig. 1B. When both bounding plates have the same director field, the disclination is shown in

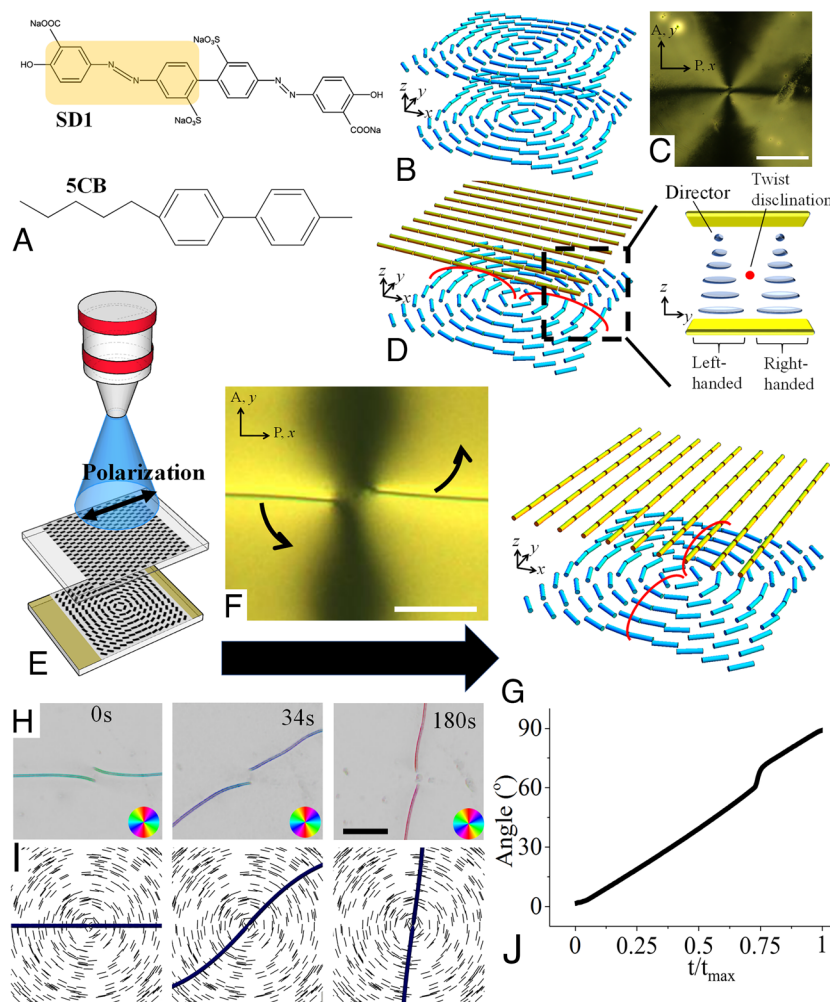


**Fig. 1.** Rotation of the disclination line due to cooperative rotation of azobenzene molecules. (A) Azobenzene SD1 molecule and nematic LC 5CB; (B) The two surfaces have the same circular orientation pattern of +1 defect; (C) Corresponding polarizing optical microscope (POM) image; (D) Disclination lines are generated along the X axis if the top substrate has a uniform alignment along the X axis; (E) A linearly polarized light is irradiated on the top substrate to induce the cooperative rotation of the azobenzene molecules; (F and G) The disclination lines will rotate with the cooperative reorganization of the azobenzene molecules (F) and reach the equilibrium state along the Y axis (G); (H) Image sequence of the rotation of the disclination lines; the color wheel represents the orientation of the line with respect to the X axis; (I) Image sequence of the numerical simulations; (J) Angular change of the orientation of the disclination line with normalized simulation time. (The scale bar is 50  $\mu$ m.)

Fig. 1C. If the top substrate is replaced with a uniform alignment along the  $x$ -axis, disclination lines will form in the direction along the  $x$ -axis (Fig. 1 D–F). Since the uniform alignment on the top surface is controlled by the organization of azobenzene molecules, their configuration can be changed by shining linearly polarized light in the direction along the  $x$ -axis (Fig. 1E). Experimentally, when the top surface is irradiated while the topological pattern on the bottom surface is frozen by the liquid crystalline polymer (*Methods*), the disclination lines start to rotate in the counterclockwise (CCW) fashion and end in the direction along the  $y$ -axis (Fig. 1 E–H and Movie S1).

To gain insight into the rotation behavior of the disclination lines, continuum simulations based on the Landau–de Gennes free energy functional are conducted (42), as shown in Fig. 1 I and J and Movie S1. In the simulation, we assume that the top surface (where there is no pattern) changes linearly from one preferred direction to another during the simulation while retaining the circular +1 defect on the bottom substrate (see *Methods* for details). During evolution, we quasi-statically equilibrated the system while continuously rotating the easy axis of the top surface from the  $x$ -axis to the  $y$ -axis and observed the rotation of the disclination line similar to the experiment (Fig. 1 I and J).

The physical underpinning is rooted in the fact that the cooperative reorganization of the azobenzene molecules on the top surface powered by light drives the collective rotation of the LC molecules close to this surface in the bulk; thus, the macroscopic rotation of the disclination lines is enabled. The large-scale rotation is due to the coupling effect of surface anchoring with cooperative rotation of self-assembled molecular motors, and rotation–rotation conversion is manifested. In this process, light, surface anchoring

(43), and viscoelastic properties (17) of the LC host are the keys to enabling the rotation of the disclination lines.

**Rotational Transport of Colloids by Light-Driven Collective Molecular Reorientations.** The rotation of the disclination lines in the rotation–rotation conversion can be utilized to transport the colloids (Fig. 2 and Movie S2). For instance, if the disclination lines at the initial stage are along the  $y$ -axis, determined by the uniform alignment along the  $y$ -axis, the disclination lines will rotate CCW under polarized-light irradiation, as shown in Fig. 2A. The disclination line ① rotates  $\pi/2$  in 140 s, Fig. 2A, i and ii, while line ② picks up a colloid at 76 s and transports the colloid following the rotatory trajectory of line ②, Fig. 2A, iii and iv. Note that line ① rotates as a curved line due to the boundary of the pattern (Fig. 2B, Inset). However, the rotation mode of line ② is modified by the colloid on the line. As shown in Fig. 2C, line ② becomes curved backward due to carrying the colloid at time  $t = 76$  s. When comparing the speed of the colloid with that of the line (Fig. 2D), the speed of the colloid is approximately half of that of the line (Fig. 2D). After 90 s, the line turns straight, and the speed of the colloid is similar to that of line ① (Fig. 2D), indicating that line ② overcomes the heaviness of the colloid with continuous light irradiation. This demonstrates the potential to transport colloids following the designed trajectories of the disclination lines by using the cooperative reconfiguration of the molecular motors.

**Transport and Self-Assembly of Colloids by Rotation–Translation Conversion.** If the bottom substrate is designed with a pattern of alternating splay-bend distortions and the top surface of a uniform alignment along the  $x$ -axis, a disclination line along the  $x$ -axis is formed (Fig. 3 A and B). If the top surface

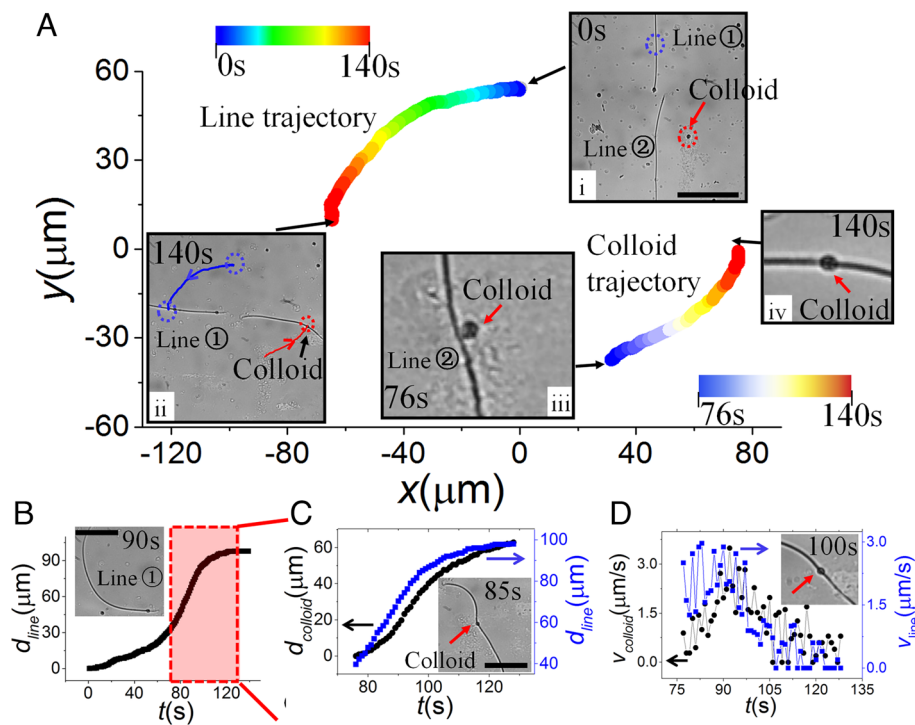


**Fig. 2.** Transport of a single colloid by rotation–rotation conversion. (A) Change of trajectories of the disclination line and colloid with time; (i) Disclination lines ① and ② at  $t = 0$  s. The tracking position on line ① is labeled by a blue circle, and the colloid is labeled by a red circle; (ii) Line ① at  $t = 140$  s; the overlaid blue and red curves are the measured trajectory of line ① and the colloid, respectively; (iii) Line ② picks up the colloid at  $t = 76$  s; (iv) Colloid on line ② reaches the final position at  $t = 140$  s; (B) Change of rotation distance  $d_{line}$  of disclination line ① with time; inset is line ① at  $t = 90$  s; (C) Comparison between time change [shaded pink region from part (B)] of distance of colloid  $d_{colloid}$  on disclination line ② (black circle) and that  $d_{line}$  of line ① (blue square); Inset is line ② carrying the colloid at  $t = 85$  s; (D) The velocity difference between the colloid  $v_{colloid}$  (black circle) and disclination line ①  $v_{line}$  (blue square) in the time span of 80 s to 140 s; Inset is the image of disclination line ② changes to straight line at  $t = 100$  s. The colloidal sphere used is 5  $\mu\text{m}$  in diameter. (The scale bar is 50  $\mu\text{m}$ .)

is irradiated with linearly polarized light along the  $x$ -axis, as shown in Fig. 3C, the disclination line shows a translational motion along the  $y$ -axis, as shown in Fig. 3D. This translation of the disclination line is attributed to the collective rotation of the LC molecules close to the top surface, which is induced by the cooperative rotation of the azobenzene molecules on that surface. Even though all the molecular motors rotate locally, their cooperative reorganization enables macroscopic rotation–translation conversion.

This effect can be used to transport the assembled colloids and help form new colloidal assemblies (Fig. 3E–J and Movie S3). As shown in Fig. 3E, there are three colloidal chains (i, ii, and iii) and three individual colloidal particles (①, ②, and ③) at  $t = 0$  s. With light irradiation, the colloidal chains move collectively following the translation of the disclination line (Fig. 3F and Movie S3). The translation distances for the three colloidal chains are shown in Fig. 3G. The amplitude of the average speed of the colloidal chains along the  $y$ -axis is  $\langle v_y \rangle = 0.38 \mu\text{m/s}$  (Fig. 3H). In addition, three individual colloids ① to ③ are picked up by the disclination line and carried forward (Fig. 3F). The calculated mean square displacement (MSD) of a single colloid transported by the disclination line shows a diffusion–advection translation along the trajectory of the disclination line following the  $y$ -axis (Fig. 3J). Interpolation of the MSD along the  $y$ -axis with  $\langle \Delta y^2 \rangle = 2D_{\text{eff}}\Delta t^v$ , where  $D_{\text{eff}}$  is the apparent diffusion constant,  $\Delta t$  is the time lag,

and  $v$  is the apparent diffusion exponent, yields  $v = 1.8 \pm 0.1$ , meaning the biased diffusion of the colloid along the  $y$ -axis and confined diffusion along the  $x$ -axis, Fig. 3J. Remarkably, the picked-up single colloid can self-assemble with the existing colloidal chain, forming a new colloidal assembly (Fig. 3I). Colloid ① is attracted to the disclination line at  $t = 11$  s and assembles with the colloidal chain at  $t = 12$  s; afterward, a new assembly with four colloidal spheres continues to be transported by the translational disclination line (Fig. 3J).

### Reversible Reconfiguration of the Self-Assembled Disclination Network

Next, we studied how the reversible cooperative rotation of azobenzene molecules induces the morphology transformation of the disclination network (Fig. 4). We start with both bounding substrates coated with the same director field of the 2D lattice of  $(+1, -1)$  defects (*Methods*), Fig. 4A. Since integer defects always split into two half-integer defects with lower elastic energy (44), the defects with topological charge of  $|m| = 1/2$  are connected by disclination lines along the  $z$ -axis (44), as shown in Fig. 4A. These disclination lines are manifested as black dots when viewed from the  $xy$ -plane at  $t = 0$  s, Fig. 4D. When the top surface is irradiated with a linear polarization along the  $y$ -axis, uniform alignment along the  $x$ -axis will be imprinted on the top surface (Fig. 4B and Movie S4). During this process, domain walls emerge at  $t = 45$  s (Fig. 4E). With time evolution, the domain

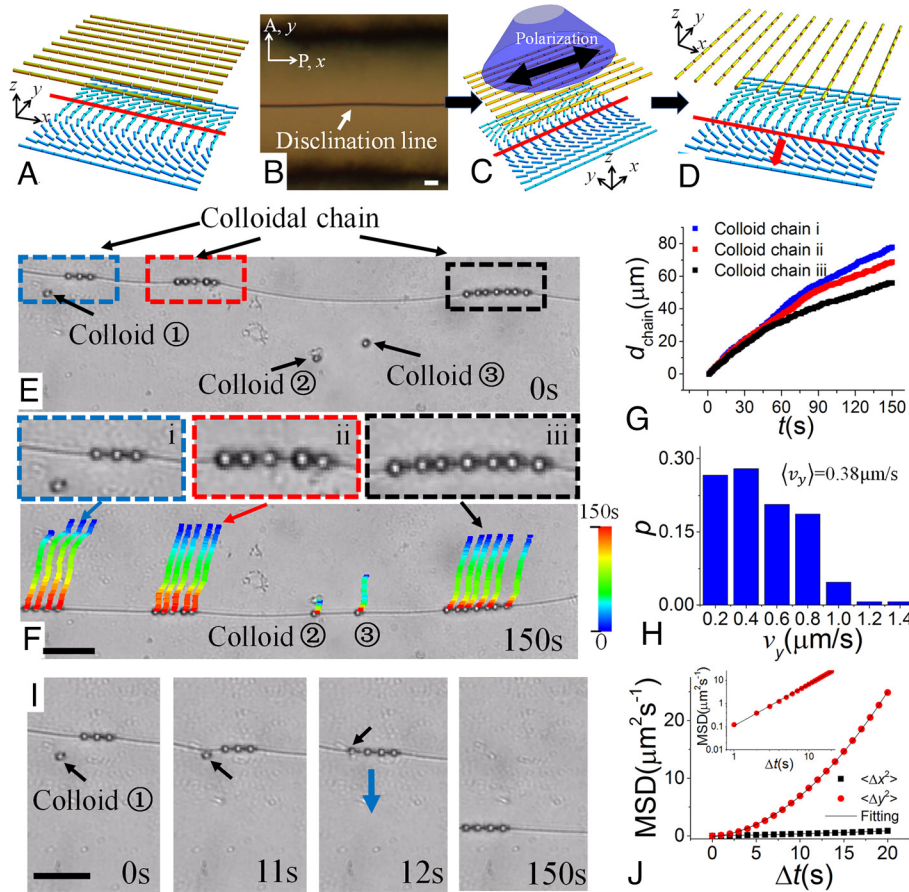


**Fig. 3.** Collective transport of colloidal assembly by rotation–translation conversion. (A) If the top substrate has a uniform alignment along the  $X$  axis and the bottom substrate is patterned with alternating splay-bend distortions, a straight disclination line is produced in the bend region; (B) Corresponding POM image; (C and D) If the top substrate is irradiated with a linear polarization along the  $X$  axis (C), the disclination line will be actuated with a translational motion along the  $Y$  axis (D); (E and F) If colloids are dispersed in this system (E), colloidal assemblies are collectively transported by the translation of the disclination line and single colloids are collected and carried forward by the line (F); (G) Translational distance of colloidal chains  $d_{\text{chain}}$  versus time; (H) Probability distribution of velocity of the colloids along  $Y$  axis,  $v_y$  and calculated average velocity  $\langle v_y \rangle = 0.38 \mu\text{m/s}$ ; (I) Detailed frames of reassembly of colloids during the translation process; (J) Biased MSD of the colloids transported by the disclination line moving along the  $Y$  axis. (The scale bar is 50  $\mu\text{m}$ .)

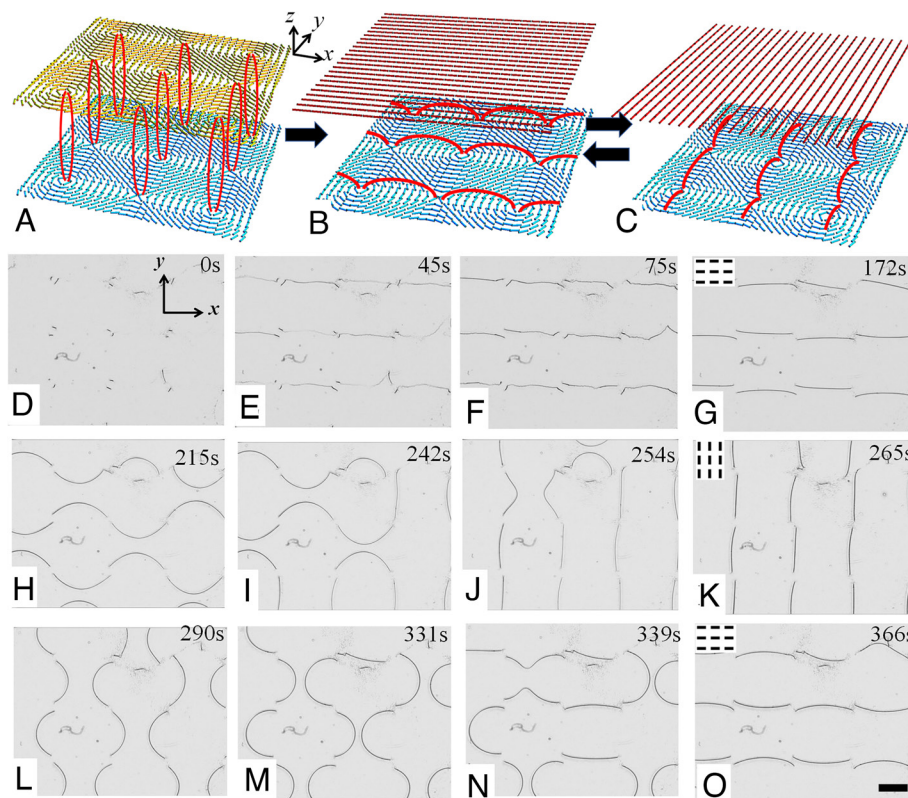


**Fig. 4.** Collective reconfiguration of the disclination network by cooperative reorganization of molecular motors. (A) When both surfaces have the same pattern of  $(+1, -1)$  defect array, the disclination lines are along  $Z$  axis; (B) If the uniform alignment along  $X$  axis is imprinted on the top surface, the disclination lines will reach the equilibrium along  $X$  axis; (C) The top surface alignment can be reversibly reconfigured by light irradiation, thus the spatiotemporal evolution of disclination network; (D–G) Experimental image sequence of dynamical reconfiguration of disclination lines when the topological pattern on the top surface is reconfigured to a uniform alignment along  $X$  axis; (H–K) Spatiotemporal evolution of disclination network if top surface alignment is changed from along  $X$  axis to  $Y$  axis; (L–O) The reversible reconfiguration when top surface alignment is changed from along  $Y$  axis to  $X$  axis. The Insets at the top left corners of G, K, and O indicate the uniform alignment on the top surface. (The scale bar is  $50 \mu\text{m}$ .)

walls transition to disclination lines (Fig. 4F and *SI Appendix*, Fig. S1), and finally, a disclination network along the  $x$ -axis is generated (Fig. 4G and *Movie S4*). Then, linearly polarized light along the  $x$ -axis is irradiated on the top surface, and the disclination lines alternatively curve upward and downward along the  $y$ -axis (Fig. 4H and *SI Appendix*, Fig. S2B). After the curved lines meet each other, they merge and immediately split into two curved disclination lines, Fig. 4 I and J and *Movie S4*. At the final stage, the disclination network is reconfigured to a network along the  $y$ -axis (Fig. 4K and *SI Appendix*, Fig. S2B), indicating that the top surface alignment is along the  $y$ -axis (Fig. 4C). Afterward, a linear polarization along the  $y$ -axis is illuminated on the top surface, and alternating curved disclination lines will relink to form a final network along the  $x$ -axis (Fig. 4 L–O), showing that the uniform alignment on the top surface is back to along the  $x$ -axis (Fig. 4B and *SI Appendix*, Fig. S2D). The reversible spatiotemporal evolution of the disclination network is due to the complex collective dynamics of the LC molecules in the bulk, which is triggered by the cooperative rotation of the azo-molecules.

In this experiment, our defect curve is a part of the wedge-twist loops (40), which has pure-twist profile in the middle and approaches wedge-twist at the two ends. As indicated by Takeuchi et al. (45),  $\pm 1/2$  defects are topologically distinct in 2D; however,  $+1/2$  wedge, twist, and  $-1/2$  wedge local profile in 3D are homeomorphic. In 3D nematics,  $\pm 1/2$  defect profiles can be connected via twist profiles through continuous transformation (44, 46).

In the middle plane of two adjacent defect curves, we have a pair of disclination lines (*SI Appendix*, Fig. S3A) with  $\pi$  rotationally symmetric director field ( $\mathbf{t}$  denotes the local tangent vector to the disclination, while the local rotation vector  $\Omega_1 = -\Omega_2$  is perpendicular to  $\mathbf{t}$ ). As the top substrate rotates, defect lines start to bend (*SI Appendix*, Fig. S3 A and B) until two neighboring curves reconnect, as shown in *SI Appendix*, Fig. S3C. The dynamics of the two disclination lines are also symmetric (*Movie S4*). After the two disclination lines connect, they split into two separated disclination lines (*SI Appendix*, Fig. S3D). A sudden jump of elastic energy from *SI Appendix*, Fig. S3 C and D is observed in the total energy (*SI Appendix*, Fig. S4) during this process. The high energy barrier between *SI Appendix*, Fig. S3 A–D reveals that rotation of top substrate can drive the transition from one defect configuration to the other which cannot be induced by thermal fluctuations.

**Reconfigurable Colloidal Assembly in Reversible Reconfiguration of the Disclination Network.** If homeotropically anchored colloids are dispersed in the above-obtained disclination network, Fig. 5A, the colloids will self-assemble on the disclination lines to minimize the free energy (30, 47), Fig. 5 B and C. Note that the uniform alignment on the top substrate is initially along the  $x$ -axis, and the colloid in the red frame in Fig. 5D is close to the  $+1$  defect. As the linear polarization along the  $x$ -axis is irradiated on the top surface, the colloidal chains tilt both upward and downward due to the curved disclination lines (Fig. 5 E and F and *Movie S5*). At the end of the evolution, the colloidal assemblies reach equilibrium

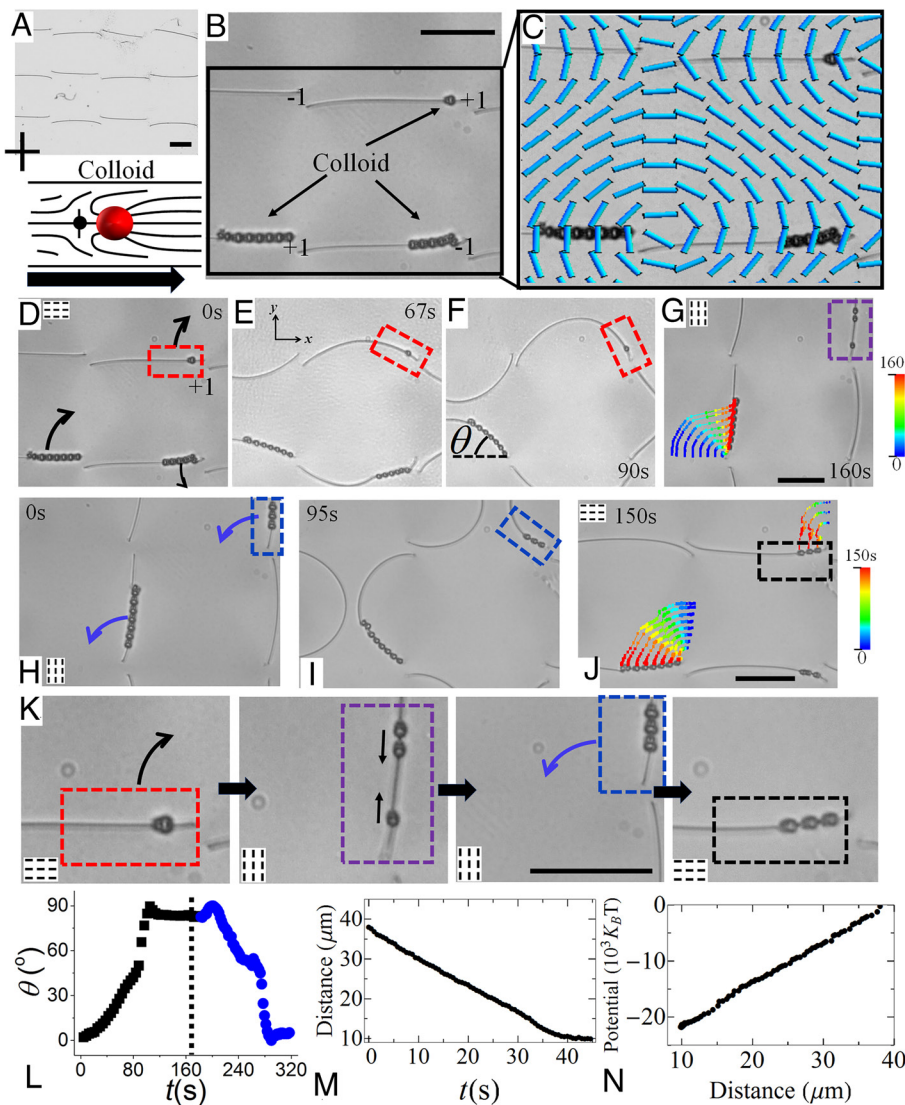


**Fig. 5.** Reconfigurable colloidal assembly in dynamic reconfiguration of disclination networks. (A) Disperse the colloidal sphere with homeotropic anchoring in the disclination network obtained from interfacing a 2D lattice of (+1, -1) defects with a uniform alignment along the  $X$  axis; (B) Colloids form linear chains on the disclination lines; (C) Enlarged image from part (B) overlaid with the director field on the bottom surface; the top surface is of the uniform alignment for light irradiation; (D–G) Image sequence of transport of colloidal assembly by the reconfiguration of disclination network; the colloidal chains are tilted with the curved disclination line; the tilting angle is shown as  $\theta$  (F); the single colloid in the red frame assembles with other two colloids from the other disclination line after the merging event of the disclination network; the colored trajectories of the colloids are shown in part (G); (H–J) Image sequence of reversible process of the disclination network carrying the colloidal assembly; (K) Zoom-in frames to show the reconfigurable assembly in the dynamic spatiotemporal evolution of the disclination network; (L) Change of the tilting angle  $\theta$  with time during this reversible process; (M) Distance between the interacting colloids versus time; (N) Interaction potential versus distance corresponding to M. The Insets at the corners indicate the uniform alignment direction on the top surface. (The scale bar is 50  $\mu\text{m}$ .)

along the  $y$ -axis, and the trajectories of the colloids are shown in Fig. 5G. After the disclination network changes to along the  $y$ -axis after the relinking events, the single colloid in the red frame will meet the colloids from the merging disclination lines, as shown in the purple frame in Fig. 5G, and a new colloidal assembly is formed (Fig. 5H). Then, if linear polarization along the  $y$ -axis is illuminated, the reversible process is triggered, and the colloidal chains will rotate from along the  $y$ -axis to the  $x$ -axis through the spatiotemporal reconfiguration of the disclination network (Fig. 5I and J and Movie S6). After the reconfiguration process of the disclination network, the disclination lines are reversibly returned to their initial position, which is manifested by the tilting angle  $\theta$  of the colloidal chain reversibly changing with time (Fig. 5L). However, the single colloid changes to a colloidal assembly composed of three colloids (black frame in Fig. 5J). The detailed frames depicting the assembly process are shown in Fig. 5K. The interactions of particles

on the same disclination line yield binding energies of approximately 20,000  $k_B T$  (Fig. 5M and N).

Interestingly, a different scenario is discovered when the colloids are initially located close to the site of the  $-1$  defect (Fig. 6A and B). In this case, as the linear polarization along the  $x$ -axis is irradiated, the disclination lines become curved, and a single colloid in the red circle is repelled by the  $-1$  defect region and moves along the disclination line to the region close to the  $+1$  defect (Fig. 6D–F and Movie S7). This behavior is markedly different from the above-discussed motion of a single colloid close to the location of the  $+1$  defect during the reconfiguration process in Fig. 5D–G. This can be understood from the elastic interaction between the dipolar colloids with the local distortion profile defined by the director field from the bottom surface pattern. As shown in Fig. 6K, the local distortion in region (i) is splay type, and the distortion around region (ii) is bend type.

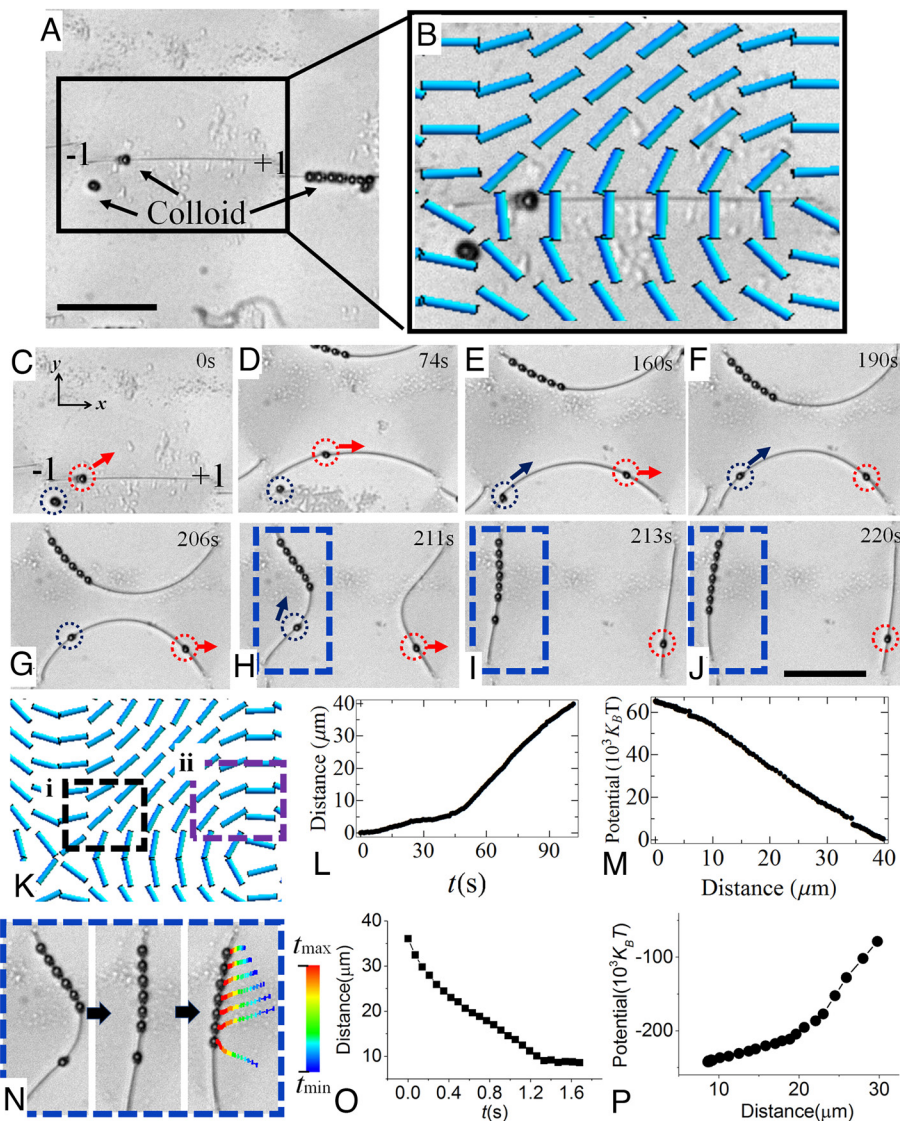


**Fig. 6.** Elasticity-mediated motion and self-assembly of the colloid on the disclination line. (A) A second scenario of colloids close to the  $-1$  defect location; (B) Enlarged image from part (A) overlaid with the director field on the bottom surface; the top surface is of the uniform alignment for light irradiation; (C–J) Image sequence of dynamics of the colloids on the disclination networks; the colloid in the red circle on the disclination line is repelled by the region of the  $-1$  defect and transported to the  $+1$  defect location (C–F); The colloid in the blue circle is attracted to the disclination line and repelled by the  $-1$  defect (E and F); Then, it is carried by the merging disclination line, and a new colloidal chain is assembled (H–J); (K) The splay (region i in black frame) and bend (region ii in purple frame) distortions close to the  $-1$  defect and  $+1$  defect, respectively; (L) Moving distance of the repelled colloid from its initial position versus time; (M) Interaction potential versus distance corresponding to L; (N) The assembly process in the blue frame of parts (H–J); The colored trajectories of moving colloids are shown in the equilibrium frame; (O and P) Interparticle distance and interaction potential during the assembly process in part (N). (The scale bar is 50  $\mu\text{m}$ .)

*SI Appendix, Fig. S5* shows that when the dipolar colloid is at its equilibrium state when attracted to the disclination line along the  $x$ -axis, the local bend distortion minimizes the elastic energy cost. If the colloid is initially close to the  $-1$  defect, as the disclination line is curved upward, *SI Appendix, Fig. S5B*, the colloid lies in the local splay distortion in region (i), *SI Appendix, Fig. S5C*. Since the local splay region (i) is not compatible with the local distortion on the left-hand side of the colloid, the elastic interaction increases the elastic energy cost and repels the colloid from region (i). As such, the colloid moves on the disclination line to the location of the  $+1$  defect. As the colloid is close to the  $+1$  defect, *SI Appendix, Fig. S5D*, the local bend region(ii) in the purple frame defined by the bottom substrate is compatible with the local distortion around the colloid, *SI Appendix, Fig. S5E*, and minimizes the elastic energy cost. Thus, the colloid reaches equilibrium following the motion of the disclination line. The

repulsive interaction potential is characterized and in the order of  $60,000 k_B T$  (Fig. 6 L and M).

Another single colloid in the blue circle that is not on the disclination line at the beginning is attracted to the disclination line after the reconfiguration starts (Fig. 6 C–E). After this colloid is located on the disclination line at  $t = 160$  s, it starts to move to the  $+1$  defect due to the same mechanism as the colloid in the red circle (Fig. 6 E–G). At  $t = 211$  s, the two adjacent disclination lines connect and split into two curved lines, resulting in the colloid in the red circle to the curved line on the right-hand side and the colloid in the blue circle to the line on the left, Fig. 6 H. Then, the colloid in the blue circle forms a new colloidal assembly with another colloidal chain from the merging disclination line (Fig. 6 H–J). The self-assembly process is detailed in the blue frame of Fig. 6 N, and the colloid–colloid interaction on the disclination line is shown in Fig. 6 O and P.

The magnitude of the interaction potential is in the order of  $10^5 k_B T$  at short distances.

**Collective Transport and Reconfiguration of Colloidal Assembly by Breaking the Symmetry of Cooperative Rotation.** As shown in Fig. 2 and *SI Appendix*, Fig. S6A, the disclination lines have equal probability of rotating in either the CCW or clockwise (CW) direction if the linear polarization  $\mathbf{P}_e$  along the  $y$ -axis is irradiated. To produce a unidirectional rotation, an extra  $\mathbf{P}_e$  along  $45^\circ$  or  $135^\circ$  with respect to the  $x$ -axis can be added to the irradiation process to induce symmetry broken. For instance, if the initial disclination lines are along the  $x$ -axis, as shown in *SI Appendix*, Fig. S6B, a  $\mathbf{P}_e$  along  $45^\circ$  is irradiated, and the lines rotate to the position shown in *SI Appendix*, Fig. S6C. Next, a  $\mathbf{P}_e$  along the  $x$ -axis is used to make the lines along the  $y$ -axis (*SI Appendix*, Fig. S6D). To produce a continuous CW rotation, a  $\mathbf{P}_e$  along  $135^\circ$  is irradiated, as shown in *SI Appendix*, Fig. S6D, and the lines reach the positions in *SI Appendix*, Fig. S6E. A final  $\mathbf{P}_e$  along the  $y$ -axis results in a unidirectional CW rotation of  $\pi$  for the disclination lines, *SI Appendix*, Fig. S6F. Likewise, by manipulating the direction of  $\mathbf{P}_e$ , a unidirectional CCW rotation of disclination lines is also enabled (*SI Appendix*, Fig. S6G–K).

As such, by using this method, collective transport of the colloidal assembly in the unidirectional CW and CCW fashions is realized, as shown in Fig. 7A–D. As shown in Fig. 7A, colloids self-assemble on the disclination line along the  $x$ -axis. The assembled colloids are

collectively transported by this disclination line in both the CW (Fig. 7B and [Movie S8](#)) and CCW (Fig. 7C and [Movie S9](#)) directions with rotation angles of  $2\pi$  and  $-2\pi$  for CCW and CW, respectively (Fig. 7D).

This success inspires us to realize the programmable reconfiguration of colloidal assembly in the experiment shown in Fig. 5. As shown in Fig. 5, a new colloidal assembly is realized during the reconfiguration of the disclination network. However, this process is reversible, and it is difficult to program the colloidal assembly by repeating the irradiations. To this end, by controlling the direction of  $\mathbf{P}_e$ , colloidal assemblies can be selectively arranged on different disclination lines (Fig. 7 E–J and [Movie S10](#)). As an example, colloidal assemblies on the disclination lines are initially formed along the  $x$ -axis (Fig. 7E). As shown in the steps of Fig. 7E and with light irradiation, the lines are curved to merge (Fig. 7E, i and ii), and colloidal assemblies are arranged on lines ① and ② along the  $y$ -axis (Fig. 7E, iii and Fig. 7F). Next, we produce new colloidal assemblies by merging line ② and line ③ which is on the right-hand side of line ② (Fig. 7G). After the merging evolution in Fig. 7G, i–iii, new colloidal assemblies are formed on lines ④ and ⑤ (Fig. 7H). By another merging event of lines ④ and ⑤, another two assemblies are produced on lines ⑥ and ⑦ (Fig. 7I and J). Following the morphological change of the disclination network, the colloidal assemblies are collectively transported and reconfigured, showing rich spatiotemporal dynamics. During these spatiotemporal evolutions, the colloidal assemblies are repelled (Fig. 7E, i and ii), broken

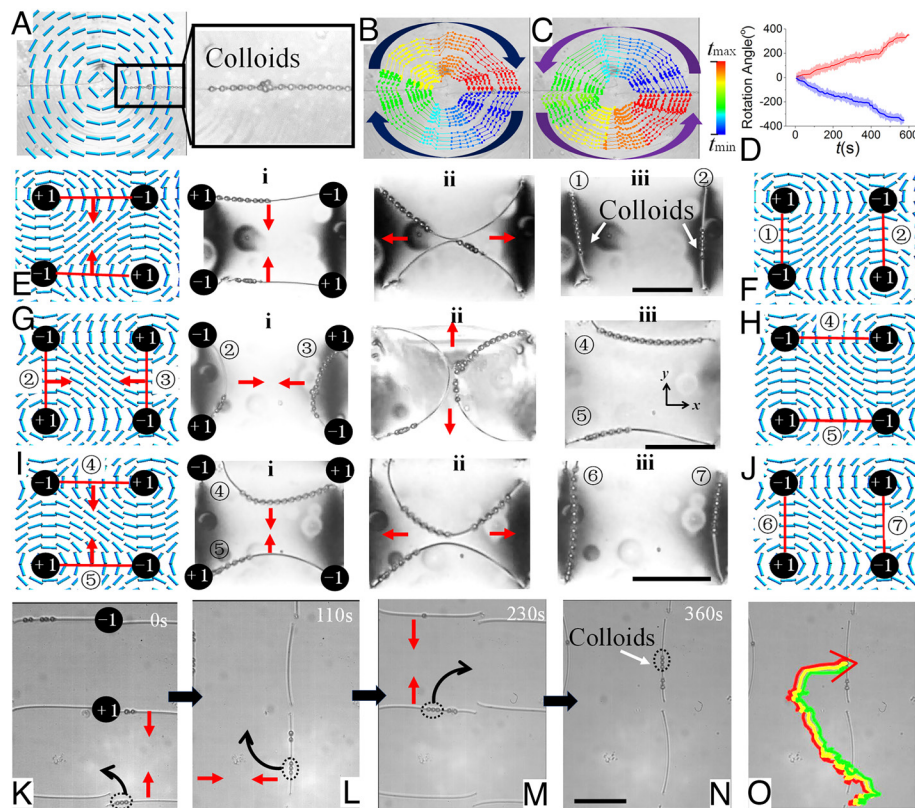


**Fig. 7.** Collective transport and reconfiguration of colloidal assemblies on the disclination lines. (A) Colloids are assembled on the disclination line; the bottom surface is of circular pattern and the top surface has the uniform alignment along  $X$  axis; (B and C) Collective transport of the colloidal assembly in both CW (B) and CCW (C) directions; (D) The colloidal assembly is unidirectionally transported with rotation angle of  $2\pi$ (CCW) and  $-2\pi$ (CW); (E) The disclination lines are merged along  $Y$  axis; the bottom surface is of 2D lattice of  $(+1, -1)$  defects and the top surface has the uniform alignment along  $X$  axis; (i–iii) are image sequence of merging event and colloidal assemblies are on lines ① and ②; red arrows indicate the moving directions of disclination lines; (F) Schematic of lines ① and ②; (G) Lines ② and ③ are merged along  $X$  axis; (i–iii) are the corresponding image sequence and colloidal assemblies are on lines ④ and ⑤ (H) Schematic of lines ④ and ⑤; (I) Lines ④ and ⑤ are merged; (i–iii) are the corresponding image sequence and colloidal assemblies are on lines ⑥ and ⑦; (J) Schematic of lines ⑥ and ⑦; (K–O) Collective transport of the colloidal chain is programmed; red arrows indicate the merging directions of disclination lines and black arrows represent the motion direction of colloidal chain; the colloidal assembly is composed of three colloids in the dotted circle; the trajectories of the three colloids are shown in O. (The scale bar is  $50 \mu\text{m}$ .)

(Fig. 7 G, ii and Fig. 7 I, ii), and combined (Fig. 7 E, iii, Fig. 7 G, iii, and Fig. 7 I, iii). The colloids are repelled due to the same mechanism of the elastic potential landscape shown in Fig. 5, and the assemblies are broken and combined because of the curvature change of the disclination lines. Likewise, the collective transport of the colloidal chain which is composed of three colloids can also be programmed by manipulating  $\mathbf{P}_e$  (Fig. 7 K–O and Movie S11). The colloidal assembly is transported following the trajectory shown in Fig. 7 O. The programmable capability can be extended to other types of defect arrays in the same experimental setting. As an example, a pattern of 2D lattice of (+1/2, -1/2) topological defects is used, *SI Appendix*, Fig. S9 and Movie S12. It shows the potential that the collective effects demonstrated in this work can be preprogrammed by topological defect designs.

## Discussion and Conclusion

Utilizing the cooperative action of molecular motors to control the macroscopic motion of microscale objects in a predesigned and programmable manner is still challenging in the areas from chemistry and materials science to physics and nanotechnology. In this work, we propose to use surface-coated azobenzene molecules to control the molecular orientations of LCs. By interfacing a spatially varying orientational pattern with a uniform alignment, both of which are imprinted in the monolayer of azo-molecules by the maskless photopatterning technique, disclination networks are produced due to the incompatibility of the preferred director fields. The azobenzene monolayer is irradiated to actuate a cooperative reorganization of the molecules on the surface, resulting in a collective motion of the LC molecules and macroscopic dynamics of the disclination network in the bulk. In this process, the spatiotemporal transformation of disclination lines is enabled by the coupling effects of input optical energy, photoisomerization of the azo-molecules, surface anchoring effect, and long-range elastic interactions of the LC molecules.

The spatiotemporal evolutions are first realized in two different manners: a) The collective rotation of azo-molecules is converted to the rotation of disclination lines if a circular pattern is used; b) The cooperative rotation of azo-molecules can also be converted to the translation of the disclination lines when a pattern of alternating distortions of bend and splay is implemented. The rotation–rotation and rotation–translation conversions are immediately applied to control the macroscopic motion of the colloidal assembly. The disclination lines and the corresponding director distortions create an elastic potential landscape for the patterning of microscale colloidal spheres to form self-assembly structures within their cores. In addition, interactions between the colloids can be tuned from attractive to repulsive by using the predesigned elastic energy landscape. From the work by Ravnik et al. (48, 49), entangled point defects were shown to build robust linear entangled chains called entangled hyperbolic defect colloidal wire. It will be interesting to decipher the director structure after the particles are trapped along the line defect in our experimental setup by using nonlinear imaging systems (50, 51). Since disclination lines formed by different topological patterns adopt a variety of topological structures (40, 45, 52, 53) and rich topologies have been demonstrated by disclination lines interacting with colloids (30, 50, 51, 54, 55), it will be intriguing to study how the coupled topological structures change during spatiotemporal reconfiguration processes in the future.

To summarize, light-driven cooperative reorganization of molecular motors induces collective motion of LC molecules and thus the morphology transformation of disclination lines formed in the LC medium, which is elucidated by continuum simulations. By

fine-tuning the topological patterns imprinted in the monolayer of azobenzene molecules, the colloids can be collectively transported, collected, and reconfigured to form new assemblies following the spatiotemporal evolution of the disclination network. In addition, the irradiated polarization can be manipulated to control the collective transport of the colloidal assembly in both unidirectional CW and CCW fashions. The colloidal assemblies can also be selectively programmed by controlling the irradiated polarization. This work offers a powerful tool to enable collective self-assembly of unique composites based on LCs and opens opportunities for new designs of smart materials and micromachines.

## Materials and Methods

**Materials.** Nematic LC 4'-pentyl-4-cyanobiphenyl (5CB) is doped with 0.01 wt% of silica colloids of radius 2.5 μm (*Cospheric Inc.*). Colloids treated with octadecyl-dimethyl-(3-trimethoxysilylpropyl) ammonium chloride (DMOAP) produce perpendicular director alignment and dipolar structures with a hyperbolic hedgehog on one side of the sphere (56). The colloidal dispersion in the LC is injected into the photopatterned cell with thickness  $h = 20 \mu\text{m}$  at room temperature 22 °C.

**Patterned Surface Alignment.** The photosensitive material azo dye SD1 was purchased from *DIC INC.* and used without further purification. SD1 was mixed with n,n-dimethylformamide solvent at a 0.2 wt% concentration. Glass substrates were washed in an ultrasonic bath with Cavi-clean detergent and then with isopropyl alcohol and dried in an oven at 80 °C for 15 min. Subsequently, the substrates were placed in a UV ozone chamber for 5 min. The SD1 solution is spin-coated on the glass substrates at 3,000 rpm for 30 s. The glass plates were baked at 95 °C for 20 min. The photosensitive azo dye on the glass substrates will be oriented perpendicular to the irradiated linearly polarized light (57). The LC director is aligned with the orientations of azo dye molecules.

The topological pattern is created by using a maskless photopatterning setup based on a projector display (38, 39). For example, a complex pattern is designed as  $\hat{\mathbf{n}} = (n_x, n_y) = (\cos\theta, \sin\theta)$ , where  $\theta(x, y) = m\tan^{-1}\frac{y}{x} + \theta_0$ ,  $m = \pm 1$  is an integer topological charge, and the phase  $\theta_0 = \pi/2$  sets the distortion with a pure bend (*SI Appendix*, Fig. S8 A and B). To create this pattern, it is divided into 36 segments, as shown in *SI Appendix*, Fig. S8C. One segment with an opening angle of 10° is taken, and both the segment and linear polarizers are set along the x-axis (*SI Appendix*, Fig. S8D). The linearly polarized light can pass through the white segment, while light from all other directions is blocked by the dark background (*SI Appendix*, Fig. S8D). Then, the rotation speed of the polarizer is  $R_1$ , and the segment is rotating at a speed of  $R_2$ . The rotation of the polarizer is controlled by a rotatory motorized stage, and the rotation of the segments is controlled by the computer. Both rotations are synchronized by a homemade LabVIEW program. For the circular pattern shown in *SI Appendix*, Fig. S8E, the ratio between  $R_1$  and  $R_2$  is defined as  $m = R_1 / R_2 = 1$ . Hence, the polarizer is rotated at speed  $R_1 = 10^6 / 10 \text{ s}$  to have a 10 s exposure time for each step. Meanwhile, the time step between two segments is 10 s. After a full  $2\pi$  rotation of segments, the circular pattern shown in *SI Appendix*, Fig. S8E will be created, as shown in *SI Appendix*, Fig. S8F. Likewise, a 2D lattice of topological defects can be produced by controlling the distance between adjacent defects. Thus, the polarization pattern of light is imprinted into the photosensitive substrate that is used to align the LC. Note that this maskless patterning technique by projecting display can produce any pattern of the director field with the typical scale of spatial gradients ranging from approximately tens of micrometers to centimeters.

**Sample Preparation.** To reduce the influence of light irradiation on the patterned substrate, an additional layer of LC polymer is coated on the top of the pattern. Monomer RM257, *SI Appendix*, Fig. S7, purchased from *Wilshire*, is mixed with toluene at a concentration of 7 wt% with photoinitiator Irgacure 651 (from *Ciba, Inc.*) at a concentration of 5 wt% of RM257. This solution was spin-coated onto the patterned SD1 substrates at 3,000 rpm for 30 s. The substrates were photopolymerized under unpolarized ultraviolet light with an intensity of  $1.4 \text{ mW/cm}^2$  for 30 min. The polymer pattern replicates the pattern of SD1 alignment beneath it.

The mixture of colloids in 5CB is injected into the cell by capillary force at 22 °C, which corresponds to the nematic phase of 5CB. After the LC filled in, the disclination lines formed, and the samples were imaged by polarizing optical

microscopy and fluorescence optical microscopy. Since the bottom substrate of the 2D topological patterns is coated with a layer of LC polymer, the bottom substrate will not be influenced by the light. The light source used to drive the sample out of equilibrium is a collimated LED (from Thorlabs) with a wavelength of 455 nm and a light intensity at the focus point of 510 mW/cm<sup>2</sup>.

**Polarizing Optical Microscopy.** We used a 50 $\times$  to 1,000 $\times$  Advanced Upright Polarized light Microscope from AmScope with both at 10 $\times$  Plan, N.A. = 0.25 objective, and 20 $\times$  Plan, N.A. = 0.40 objective. Optical microscopic images were captured by a 20MP USB3.0 BSI C-mount Microscope Camera from AmScope. (resolution 5,440  $\times$  3,648 pixels).

**Disclination Line Orientational Angle Measurement.** Micrographs are processed by ImageJ, and the directionality of the disclination lines is measured at the lines of interest (LOIs). Each data point in the profile represents the orientational angle of the disclination line in the LOI. The color on the disclination line represents the orientational angle of the line.

**Characterization of Colloidal Transport and Pair Interactions.** The motion of the disclination lines and colloids is processed by tracking the displacement of their motion using ImageJ MTrackJ Plugin. To calculate the rotation angle of the transported colloidal assembly, each step of the trajectory is measured as  $(x_i, y_i)$ , and the center of the defect is  $(x_0, y_0)$ . The distance between each step and the center of the defect is  $\sqrt{(x_i - x_0)^2 + (y_i - y_0)^2}$ . The rotational angles are calculated as  $\arcsin(|y_i - y_0| / \sqrt{(x_i - x_0)^2 + (y_i - y_0)^2})$ . Depending on the quadrant of the colloid lies in,  $\pi/2$ ,  $\pi$ , and  $3\pi/2$  are added to the calculated angle for each particle.

Since the Reynolds number in our system is much smaller than 1, the colloidal system is highly overdamped. Hence, the inertia effects are negligible and the elastic interaction forces are balanced by the viscous drag forces. To calculate the interaction potential, the time dependence of the distance that the colloids travel is determined by tracking their trajectories. Following Stokes' law, the viscous drag force  $f_d = 6\pi R\eta_{eff} \partial r / \partial t$  is balanced by the elastic force mediated by the surrounding medium (56), where  $R = 2.5 \mu\text{m}$  is the particle radius,  $\eta_{eff} = (\eta_{||} + \eta_{\perp})/2$  is chosen to be the effective viscosity, and  $\partial r / \partial t$  is the speed of the colloid.  $\eta_{||} = 63.5 \text{ mPa}\cdot\text{s}$  and  $\eta_{\perp} = 90.0 \text{ mPa}\cdot\text{s}$  are two characteristic viscosities of 5CB (58). The distance dependence of the interaction potential can be calculated by integrating the calculated drag force (59).

**Theoretical Model of Numerical Simulations.** The total free energy  $F$  of a nematic LC is given by

$$F = \int_V (f_{LdG} + f_{el} + f_{surf}) dV + \int_S f_s dS, \quad [1]$$

where  $f_{LdG}$  is the short-range Landau-de Gennes free energy,  $f_{el}$  is the long-range elastic energy, and  $f_{surf}$  is the surface anchoring-induced free energy. The Landau-de Gennes free energy density  $f_{LdG}$  takes the form (17)

$$f_{LdG} = \frac{A_0}{2} \left( 1 - \frac{U}{3} \right) \text{Tr}(\mathbf{Q}^2) - \frac{A_0 U}{3} \text{Tr}(\mathbf{Q}^3) + \frac{A_0 U}{4} \text{Tr}(\mathbf{Q}^2)^2, \quad [2]$$

where  $\mathbf{Q}$  is the tensorial order parameter from an ensemble average over unit vector  $\mathbf{n}$  (representing the molecular orientation),  $\mathbf{Q} = \langle \mathbf{n}\mathbf{n} - \mathbf{I}/3 \rangle$ . Parameter  $U$  controls the magnitude of  $S$  of a homogenous static system through

$$S = \frac{1}{4} + \frac{3}{4} \sqrt{1 - \frac{8}{3U}}. \quad [3]$$

The Frank-Oseen elastic free energy density for the nematic LC is expressed as (60)

$$f_{el}^{FO} = \frac{1}{2} K_1 (\nabla \cdot \mathbf{n})^2 + \frac{1}{2} K_2 (\mathbf{n} \cdot \nabla \times \mathbf{n})^2 + \frac{1}{2} K_3 (\mathbf{n} \times (\nabla \times \mathbf{n}))^2 - \frac{1}{2} K_{24} \nabla \cdot [\mathbf{n}(\nabla \cdot \mathbf{n}) + \mathbf{n} \times (\nabla \times \mathbf{n})], \quad [4]$$

where  $K_1$ ,  $K_2$ ,  $K_3$ , and  $K_{24}$  are the splay, twist, bend, and saddle-splay elastic moduli, respectively. To be consistent with the Landau-de Gennes energy, elastic

energy density in the simulation is alternatively written in terms of the  $\mathbf{Q}$ -tensor (in Einstein summation form)

$$f_{el}^Q = \frac{1}{2} L_1 (\partial_k Q_{ij}) (\partial_k Q_{ij}) + \frac{1}{2} L_2 (\partial_k Q_{jk}) (\partial_l Q_{jl}) + \frac{1}{2} L_3 Q_{ij} (\partial_i Q_{kl}) (\partial_j Q_{kl}) + \frac{1}{2} L_4 (\partial_l Q_{jk}) (\partial_k Q_{jl}). \quad [5]$$

The mapping between constant sets  $K_1, K_2, K_3, K_{24}$  and  $L_1, L_2, L_3, L_4$  is

$$\begin{aligned} L_1 &= \frac{1}{2S^2} \left[ K_2 + \frac{1}{d}(K_3 - K_1) \right], \\ L_2 &= \frac{1}{S^2} (K_1 - K_{24}), \\ L_3 &= \frac{1}{2S^3} (K_3 - K_1), \\ L_4 &= \frac{1}{S^2} (K_{24} - K_2). \end{aligned} \quad [6]$$

The anchoring energy  $f_{surf}$  is calculated by the nondegenerate formula, the so-called Rapini-Papoular form (42)

$$f_s = \frac{1}{2} W (\mathbf{Q} - \mathbf{Q}_s)^2, \quad [7]$$

where  $\mathbf{Q}_{surf}$  is the preferred field of the surface,  $\mathbf{Q}_{surf} = S(\mathbf{n}_s \mathbf{n}_s - \mathbf{I}/3)$ ,  $\mathbf{n}_s$  is the surface-preferred molecular orientation, and  $W$  is the anchoring strength. In our simulation, we have assumed that  $\mathbf{Q}_{surf}$  of the top surface (where there is no pattern) changes linearly from one preferred direction to another during the simulation, represented by the change of angle  $\varphi$ . After equilibrating the initial state, all rotations are run for a total number of steps of 250,000 to ensure that the systems will be evolving quasi-statically. Eq. 1 constructs a thermodynamic potential that determines the stable or metastable solutions of the system. We define a molecular field

$$\mathbf{H} = - \left[ \frac{\delta F}{\delta \mathbf{Q}} \right]^{st}, \quad [8]$$

where  $[...]^{st}$  is a symmetric and traceless operator. Assuming that all transitions are quasi-static processes, the evolution of the  $\mathbf{Q}$ -tensor for bulk points follows

$$\partial_t \mathbf{Q} = \Gamma_s \mathbf{H}, \quad [9]$$

where  $\Gamma_s$  is the relaxation constant. For surface points, the evolution of  $\mathbf{Q}$  follows, where  $[...]^{st}$  is a symmetric and traceless operator.  $t$  is the relaxation step. Constant  $L_1 = 4 \times 10^{-11} \text{ N}$ ,  $L_2 = 4 \times 10^{-11} \text{ N}$ ,  $L_3 = 2.88 \times 10^{-11} \text{ N}$ , and  $L_4 = 0$ . The numerical parameters used here are  $A_0 = 1.17 \times 10^5 \text{ J/m}^3$ ,  $U = 3.5$ . To simulate 4'-pentyl-4-cyanobiphenyl (5CB), elastic constants are  $K_1 = 6 \text{ pN}$ ,  $K_2 = 3.9 \text{ pN}$ ,  $K_3 = 8.2 \text{ pN}$ , and  $K_{24} = 7 \text{ pN}$ . We used a random director field as the initial condition. The characteristic length scale is set to the nematic coherence length, the defect core size, with  $\xi_N = \sqrt{L_1/A_0} \approx 6.63 \text{ nm}$ .

**Defect Patterns in Numerical Simulations.** In this study, we analyzed several topological patterns on the bottom substrate. The nematic is described by a director field  $(n_x, n_y, n_z)$ . The simulation box size is  $[Nx, Ny, Nz]$ . In the simulation parts in Fig. 4, we introduce a bottom surface pattern consisting of a lattice of topological defects. The preferred director field  $\mathbf{n}_s$  at each surface point is determined by all the surface defects. For each defect  $i$  of topological charge  $c_i$ , the preferred surface orientation  $\mathbf{n}_s \propto \sum_i e^{-cr} (\cos(c_i \arctan(y - y/x - x_i) + \theta_i), \sin(c_i \arctan(y - y/x - x_i) + \theta_i), 0)$  is a superposition of vectors weighted by an exponential function of the distance  $r$  between defect  $i$  and the point of interest with a relative position vector  $(x, y, 0)$ , where  $\theta_i$  is the direction of charge  $i$  and constant  $c$  is set to  $Nx/1,000$ .

The bottom substrate of Fig. 1 has a circular ring pattern. We assume that the director varies continuously. In the circular pattern, let the bottom director at the center of the bottom substrate be  $\theta_1$  and the bottom director at the edge of the substrate be  $\theta_2$ ; thus,  $\mathbf{n}_s$  is  $\left( \cos\left(\theta_1 + \frac{\sqrt{x^2 + y^2}}{\sqrt{Nx^2 + Ny^2}} \theta_2\right), \sin\left(\theta_1 + \frac{\sqrt{x^2 + y^2}}{\sqrt{Nx^2 + Ny^2}} \theta_2\right), 0 \right)$ .

**Data, Materials, and Software Availability.** All study data are included in the article and/or *SI Appendix*.

**ACKNOWLEDGMENTS.** R.Z. acknowledges the Hong Kong Research Grants Council grant no. 26302320.

- Author affiliations: <sup>a</sup>Department of Physics, University of Science and Technology of China, Hefei, Anhui 230026, China; <sup>b</sup>Department of Physics, The Hong Kong University of Science and Technology, Clear Water Bay, Kowloon, Hong Kong 99999, China; and <sup>c</sup>Department of Physics and Materials Science, The University of Memphis, Memphis, TN 38152
1. R. Milo, R. Phillips, *Cell Biology by the Numbers* (Taylor & Francis, New York, 2015).
  2. D. Bray, *Cell Movements: From Molecules to Motility* (Taylor & Francis, New York, 2000).
  3. E. J. Cohen, J. L. Ferreira, M. S. Ladinsky, M. Beeby, K. T. Hughes, Nanoscale-length control of the flagellar driveshaft requires hitting the tethered outer membrane. *Science* **356**, 197 (2017).
  4. Y. Chang *et al.*, Molecular mechanism for rotational switching of the bacterial flagellar motor. *Nat. Struct. Mol. Biol.* **27**, 1041 (2020).
  5. K. L. Weirich, K. Dasbiswas, T. A. Witten, S. Vaikuntanathan, M. L. Gardel, Self-organizing motors divide active liquid droplets. *Proc. Natl. Acad. Sci. U.S.A.* **116**, 11125 (2019).
  6. A. P. Davis, Synthetic molecular motors. *Nature* **401**, 120 (1999).
  7. M. Schliwa, G. Woehlke, Molecular motors. *Nature* **422**, 759 (2003).
  8. V. Balzani, M. Venturi, A. Credi, *Molecular Devices and Machines: A Journey into the Nanoworld* (John Wiley & Sons, Weinheim, 2006).
  9. S. Erbas-Cakmak, D. A. Leigh, C. T. McLernan, A. L. Nussbaumer, Artificial molecular machines. *Chem. Rev.* **115**, 10081 (2015).
  10. T. R. Kelly, H. De Silva, R. A. Silva, Unidirectional rotary motion in a molecular system. *Nature* **401**, 150 (1999).
  11. N. Koumura, R. W. Zijlstra, R. A. Van Delden, N. Harada, B. L. Feringa, Light-driven monodirectional molecular rotor. *Nature* **401**, 152 (1999).
  12. D. A. Leigh, J. K. Wong, F. Dehez, F. Zerbetto, Unidirectional rotation in a mechanically interlocked molecular rotor. *Nature* **424**, 174 (2003).
  13. T. Kudernac *et al.*, Electrically driven directional motion of a four-wheeled molecule on a metal surface. *Nature* **479**, 208 (2011).
  14. R. Eelkema *et al.*, Molecular machines: Nanomotor rotates microscale objects. *Nature* **440**, 163 (2006).
  15. M. E. J. Friese, T. A. Nieminen, N. R. Heckenberg, H. Rubinsztein-Dunlop, Optical alignment and spinning of laser-trapped microscopic particles. *Nature* **394**, 348 (1998).
  16. B. L. Feringa, "Chiroptical Molecular Switches and Motors". *Molecular Photoswitches: Chemistry, Properties, and Applications* (John Wiley & Sons, Weinheim, 2022), vol. 2.
  17. P. G. de Gennes, J. Prost, *The Physics of Liquid Crystals* (Clarendon, Oxford, 1993).
  18. M. Zapotocky, L. Ramos, P. Poulin, T. C. Lubensky, D. A. Weitz, Particle-stabilized defect gel in cholesteric liquid crystals. *Science* **283**, 209 (1999).
  19. M. Yada, J. Yamamoto, H. Yokoyama, Direct observation of anisotropic interparticle forces in nematic colloids with optical tweezers. *Phys. Rev. Lett.* **92**, 185501 (2004).
  20. I. I. Smalyukh, O. D. Lavrentovich, A. N. Kuzmin, A. V. Kachynski, P. N. Prasad, Elasticity-mediated self-organization and colloidal interactions of solid spheres with tangential anchoring in a nematic liquid crystal. *Phys. Rev. Lett.* **95**, 157801 (2005).
  21. I. Mušević, M. Škarabot, U. Tkalec, M. Ravnik, S. Žumer, Two-dimensional nematic colloidal crystals self-assembled by topological defects. *Science* **313**, 954 (2006).
  22. M. Ravnik *et al.*, Entangled nematic colloidal dimers and wires. *Phys. Rev. Lett.* **99**, 247801 (2007).
  23. U. Ognysta *et al.*, 2D interactions and binary crystals of dipolar and quadrupolar nematic colloids. *Phys. Rev. Lett.* **100**, 217803 (2008).
  24. T. A. Wood, J. S. Lintuvuori, A. B. Schofield, D. Marenduzzo, W. C. K. Poon, A self-quenched defect glass in a colloid-nematic liquid crystal composite. *Science* **334**, 79 (2011).
  25. A. Martinez, H. C. Mireles, I. I. Smalyukh, Large-area optoelastic manipulation of colloidal particles in liquid crystals using photoresponsive molecular surface monolayers. *Proc. Natl. Acad. Sci. U.S.A.* **108**, 20891 (2011).
  26. R. P. Trivedi, I. I. Klevets, B. Senyuk, T. Lee, I. I. Smalyukh, Reconfigurable interactions and three-dimensional patterning of colloidal particles and defects in lamellar soft media. *Proc. Natl. Acad. Sci. U.S.A.* **109**, 4744 (2012).
  27. B. I. Senyuk *et al.*, Topological colloids. *Nature* **493**, 200 (2013).
  28. C. Blanc, D. Coursault, E. Lacaze, Ordering nano- and microparticles assemblies with liquid crystals. *Liq. Cryst. Rev.* **1**, 83 (2013).
  29. H. Mundoor, B. Senyuk, I. I. Smalyukh, Triclinic nematic colloidal crystals from competing elastic and electrostatic interactions. *Science* **352**, 69 (2016).
  30. I. Mušević, *Liquid Crystal Colloids* (Soft and Biological Matter, Springer, Switzerland, Cham, 2017).
  31. W. R. Browne, B. L. Feringa, Making molecular machines work. *Nat. Nanotechnol.* **1**, 25 (2006).
  32. Y. Yuan, G. N. Abuhamed, Q. Liu, I. I. Smalyukh, Self-assembled nematic colloidal motors powered by light. *Nat. Commun.* **9**, 5040 (2018).
  33. Y. Yuan, Q. Liu, B. Senyuk, I. I. Smalyukh, Elastic colloidal monopoles and reconfigurable self-assembly in liquid crystals. *Nature* **570**, 214 (2019).
  34. A. Eremin *et al.*, Optically driven translational and rotational motions of microrod particles in a nematic liquid crystal. *Proc. Natl. Acad. Sci. U.S.A.* **112**, 1716 (2015).
  35. A. Ryabchuk *et al.*, Helix inversion controlled by molecular motors in multistate liquid crystals. *Adv. Mater.* **32**, 2004420 (2020).
  36. R. Thomas, Y. Yoshida, T. Akasaka, N. Tamaoka, Influence of a change in helical twisting power of photoresponsive chiral dopants on rotational manipulation of micro-objects on the surface of chiral nematic liquid crystalline films. *Chem. A Eur. J.* **18**, 12337 (2012).
  37. L.-L. Ma *et al.*, Programmable self-propelling actuators enabled by a dynamic helical medium. *Sci. Adv.* **7**, eabb3505 (2021).
  38. J. Chen *et al.*, Nematic templated complex nanofiber structures by projection display. *ACS Appl. Mater. Interfaces* **14**, 7230 (2022).
  39. J. Chen, O. I. Akomolafe, J. Jiang, C. Peng, Light-actuated liquid crystal elastomer prepared by projection display. *Materials* **14**, 7245 (2021).
  40. J. Jiang *et al.*, Active transformations of topological structures in light-driven nematic disclination networks. *Proc. Natl. Acad. Sci. U.S.A.* **119**, e212226119 (2022).
  41. Y. Guo *et al.*, Photopatterned designer disclination networks in nematic liquid crystals. *Adv. Opt. Mater.* **9**, 2100181 (2021).
  42. M. Ravnik, Š. Žumer, Landau-de Gennes modelling of nematic liquid crystal colloids. *Liq. Cryst.* **36**, 1201 (2009).
  43. O. Yaroshchuk, Y. Reznikov, Photocalignment of liquid crystals: Basics and current trends. *J. Mater. Chem.* **22**, 286 (2012).
  44. M. Kleman, O. D. Lavrentovich, *Soft Matter Physics: An Introduction* (Springer-Verlag, New York Inc, United States, 2003), p. 637.
  45. Y. Zushi, K. A. Takeuchi, Scaling and spontaneous symmetry restoring of topological defect dynamics in liquid crystal. *Proc. Natl. Acad. Sci. U.S.A.* **119**, e207349119 (2022).
  46. G. Duclos *et al.*, Topological structure and dynamics of three-dimensional active nematics. *Science* **367**, 1120 (2020).
  47. D. Pires, J.-B. Fleury, Y. Galerne, Colloid particles in the interaction field of a disclination line in a nematic phase. *Phys. Rev. Lett.* **98**, 247801 (2007).
  48. M. Ravnik, Š. Žumer, Nematic braids: 2D entangled nematic liquid crystal colloids. *Soft Matter* **5**, 4520 (2009).
  49. M. Ravnik, Ž. Slobodan, Nematic colloids entangled by topological defects. *Soft Matter* **5**, 269 (2009).
  50. I. I. Smalyukh, Liquid crystal colloids. *Annu. Rev. Condensed Matter Phys.* **9**, 207 (2018).
  51. I. I. Smalyukh, Review: Knots and other new topological effects in liquid crystals and colloids. *Rep. Prog. Phys.* **83**, 106601 (2020).
  52. N. Petit-Garrido *et al.*, Healing of defects at the interface of nematic liquid crystals and structured langmuir-blodgett monolayers. *Phys. Rev. Lett.* **107**, 177801 (2011).
  53. C. Meng, J.-S. Wu, I. I. Smalyukh, Topological steering of light by nematic vortices and analogy to cosmic strings. *Nat. Mater.* **22**, 64 (2023).
  54. U. Tkalec, I. Mušević, Topology of nematic liquid crystal colloids confined to two dimensions. *Soft Matter* **9**, 8140 (2013).
  55. U. Tkalec, M. Ravnik, S. Čopar, S. Žumer, I. Mušević, Reconfigurable knots and links in chiral nematic colloids. *Science* **333**, 62 (2011).
  56. C. Peng *et al.*, Control of colloidal placement by modulated molecular orientation in nematic cells. *Sci. Adv.* **2**, e1600932 (2016).
  57. C. Peng, T. Turiv, Y. Guo, Q.-H. Wei, O. D. Lavrentovich, Command of active matter by topological defects and patterns. *Science* **354**, 882 (2016).
  58. T. Turiv *et al.*, Effect of collective molecular reorientations on Brownian motion of colloids in nematic liquid crystal. *Science* **342**, 1351 (2013).
  59. M. Škarabot *et al.*, Laser trapping of low refractive index colloids in a nematic liquid crystal. *Phys. Rev. E* **73**, 021705 (2006).
  60. I. W. Stewart, *The Static and Dynamic Continuum Theory of Liquid Crystals: A Mathematical Introduction* (CRC Press, Boca Raton, 2019).